Passive Sensing for Internet of Medical Things: A Low-Cost Batteryless Wearable Sweat Rate Sensor

Sergio López-Soriano, *Member, IEEE*, Josep Parrón-Granados, and Joan Meliá-Seguí, *Senior Member, IEEE*

***Abstract*—Continuous monitoring of the sweat rate can support the early diagnosis of several chronic diseases, such as Parkinson's or diabetes. However, current wearable wireless devices use batteries that have a limited operating time, also increasing their cost, and thus, reducing their accessibility to a large part of the population. In that sense, passive IoT technologies could be exploited to produce battery-less low-cost antenna-based sensors (ABSs). In this article, we propose an ultrahigh frequency (UHF) radiofrequency identification (RFID) battery-less ABS that transforms the amount of sweat accumulated inside a microfluidic channel into a variation of the tag response. In order to provide multilevel sensing, we rely on the integrated circuit self-tuning sensor code, which is passively backscattered to the reader unit, instead of channel information which may provide insufficient resolution depending on the geographical location. The sensor performance is validated experimentally, achieving an accuracy of 90% in the estimation of the sweat loss and 95% in the estimation of the average sweat rate.**

***Index Terms*—Antenna-based sensor (ABS), microfluidics, radiofrequency identification (RFID), sweat loss, sweat rate.**

I. INTRODUCTION

THE Internet of Medical Things (IoMT) provides remote patient monitoring enabling real-time tracking of chronic conditions and early detection of potential health issues [1]. Wearable sensors play a crucial role in the IoMT by collecting data from the human body or medical environments [2], [3], [4]. These devices can measure a range of physiological parameters and environmental factors, including biomarkers that are present in the human sweat [5]. Sweat loss measuring devices (SLMD) can help in the early diagnosis of several chronic diseases, thermoregulatory disorders and illnesses related to heat stress [6]. In addition, the sweat rate must be carefully monitored to produce accurate analysis of other sweat biomarkers [7].

Wearable electronic SLMD are power-hungry devices [8], [9]. They require the use of batteries to power on their electronic components. However, battery life is limited and needs to be replaced once it runs out. Therefore, these devices require human supervision to produce continuous measurements. In addition, the constant need for battery replacement increases the costs and the environmental impact associated with battery production and disposal. All of the above reduces this technology accessibility to large parts of the population, specially impacting population at risk in developing countries with high temperatures.

Backscattering technologies can support massive deployment of IoMT devices at low operational cost [10]. Ultrahigh frequency (UHF) radiofrequency identification (RFID) antenna-based sensors (ABSs) can potentially enable battery-less and low-cost SLMD. However, traditional methods [11] present several drawbacks: 1) low accuracy associated with the poor linearity of the sensor response; 2) the sensor must keep the same position and orientation with respect to the reader unit for the duration of a complete measurement cycle (≈30 s); and 3) the frequency bandwidth limitations impose strict constraints in terms of the sensor range and resolution. These methods will hereinafter be referred to as frequency shift tracking (FST) methods. In consequence, antenna-based SLMD have not been developed to date.

RFID sensors relying on self-tuning integrated circuits (ICs) [12], [13], [14], [15] can help overcoming some of the previous drawbacks by improving the sensor linearity, reducing the impact of the human movement in the sensor measurement due to the much faster acquisition procedure at the sensor side ($T_r < 1$ s), and increasing the measurement resolution by enabling up to 500 different sensing levels [16]. Methods based on ICs self-tuning mechanisms will hereinafter be referred to as capacitance shift tracking (CST) methods.

In the last years, microfluidic systems have been used in wearable devices for sweat rate monitoring [7], [17] and radiofrequency-based sensing devices for the analysis of liquids [18] and flow monitoring [19]. An early research [20] combined microfluidic channels with a meandered line antenna (MLA) to detect 1% water in ethanol using an RFID tag.

Received 7 October 2024; accepted 3 December 2024. Date of publication 12 December 2024; date of current version 9 April 2025. This work was supported in part by the Spanish Ministry of Science, Innovation and Universities through RF-VOLUTION Project under Grant PID2021-122247OB-I00 and through MATILDE Project under Grant PID2021-127203OB-I00; in part by the Generalitat de Catalunya through Suport a Grups de Recerca (SGR) Funds under Grant 2021-SGR-00174; in part by the TECNIO EXP under Grant URD250/23; and in part by the eHealth Center (Universitat Oberta de Catalunya) through a Proof of Concept Grant. *(Corresponding author: Sergio López-Soriano.)*

Sergio López-Soriano is with the Internet Interdisciplinary Institute, Universitat Oberta de Catalunya, 08018 Barcelona, Spain (e-mail: slopezsor@uoc.edu).

Josep Parrón Granados is with the Department of Telecommunication and Systems Engineering, Universitat Autónoma de Barcelona, 08193 Bellaterra, Spain (e-mail: josep.parron@uab.cat).

Joan Meliá-Seguí is with the Faculty of Computer Science, Multimedia and Telecommunications, Universitat Oberta de Catalunya, 08018 Barcelona, Spain (e-mail: melia@uoc.edu).

Digital Object Identifier 10.1109/JIOT.2024.3514298

© 2024 The Authors. This work is licensed under a Creative Commons Attribution 4.0 License.
For more information, see https://creativecommons.org/licenses/by/4.0/

A patch antenna with an embedded microfluidic channel is used to quantify the moisture content in lubricating oil [21]. A recent work [22] reports an RFID flow sensor consisting of a T-matched MLA with a stacked microfluidic paper trace that enables the detection of five volume levels. However, current developments do not provide the sensor range, resolution, and accuracy required for sweat rate monitoring.

This work introduces the first antenna-based SLMD that combines high sensing accuracy with an energy-efficient and low-cost solution. The proposed solution consists of an ABS, including a microfluidic channel and connected to a commercial off-the-shelf self-tuning UHF RFID IC. A methodology for obtaining the sweat loss and sweat rate measurements using FST and CST methods is derived in Section II. Section III includes the presentation of the proposed ABS design, a parametric analysis providing the design guidelines for constrained optimization, and the analysis of the sensor operation through simulations. Section IV presents the fabricated prototype and the laboratory measurements using a vector network analyzer (VNA) and a syringe pump injecting the artificial sweat into the sensor microfluidic channel. In this section, the FST and CST methods are compared. Section V describes multiflow rate laboratory experiments conducted using a commercial RFID reader, read range measurements with the Tagformance Pro [23], and a realistic experiment using a commercial RFID reader. The results show that the presented solution has potential for enabling cost-efficient remote patient monitoring services, allowing the democratization of SLMD. Finally, the conclusions of this work are summarized in Section VI.

II. METHODS

In this section, the theoretical background required for the estimating the sweat loss and sweat rate using the FST and CST methods is derived for the first time to the best of the authors' knowledge.

A. Sensing Methods

The FST method tracks the frequency ($\hat{f}$) corresponding to the peak or notch of a tag performance metric $\Psi = \{\tau, G\tau, P_{to}, R_r\}$, where τ is the power transmission coefficient [24], $G\tau$ is the tag realised gain [25], P_{to} is the turn-on power [26], and R_r is the read range [25]. These tag performance metrics depend on the complex conjugate impedance matching between the tag antenna impedance $Z_a(f, V)$ and the IC impedance $Z_{IC}(f, C_0)$, where f is the measurement frequency, V is the sweat volume of the microfluidic channel, and C_0 is a fixed capacitance value. Therefore, $\hat{f}$ can be expressed as

$$\hat{f} = \underset{f \in [f_{\min}, f_{\max}]}{\arg\max} \; \Psi(f, V, C_0). \tag{1}$$

Then, $\hat{f}$ can be mapped to the local sweat rate q [27] which is defined as the sweat volume entering the microfluidic channel during a time interval. For an infinitesimally small time interval, it can be computed as

$$q\left(\hat{f}, t\right) = \frac{dV}{dt} = \frac{dV}{d\hat{f}} \cdot \frac{d\hat{f}}{dt} = S_{\mathrm{FST}}^{-1} \cdot \frac{d\hat{f}}{dt} \tag{2}$$

where S_{FST} is the sensor sensitivity for the FST method. The sweat loss, V, is obtained multiplying by dt and integrating at both sides as

$$V(f) = S_{\mathrm{FST}}^{-1} \cdot \left(\hat{f} - \hat{f}(V_{\min})\right). \tag{3}$$

The CST method consists of finding the sensor code associated with the capacitance value $\hat{C}$ for which the IC receives the highest power from the antenna for a specific operation frequency, f_0. In this case, the sensor state can be described as $Z_a(f_0, V)$ and the IC state as $Z_{IC}(f = f_0, C)$, where $C \in C_{\min}, C_{\max}$ belongs to the interval of values that the self-tuning mechanism can provide. The process of finding the optimal $\hat{C}$ is entirely conducted at the IC and can be expressed as

$$\hat{C} = \underset{C \in [C_{\min}, C_{\max}]}{\arg\max} \; \Psi(f_0, V, C). \tag{4}$$

Analogous to the FST method, the local sweat loss using the CST method is given by

$$V\left(\hat{C}\right) = S_{\mathrm{CST}}^{-1} \cdot \left(\hat{C} - \hat{C}(V_{\min})\right) \tag{5}$$

where $S_{\mathrm{CST}} = ([d\hat{C}]/[dV])$ is the sensor sensitivity for the CST method. The sweat rate is computed as

$$q\left(\hat{C}, t\right) = \frac{\Delta V}{\Delta t} = S_{\mathrm{CST}}^{-1} \cdot \frac{\hat{C}_k - \hat{C}_{k-\Delta k}}{t_k - t_{k-\Delta k}} \tag{6}$$

where k is the measurement subindex.

B. Sensor Range and Resolution

The sensor range and resolution in terms of the sweat loss and sweat rate are defined next.

When the sweat loss is considered, the sensor range, $\Delta V_{\max}$, is equal to the volume of the microfluidic channel (V_{ch}). In the case of the FST method, the sensor bandwidth is set to 52 channels with separations of $\Delta f_{\min} = 500$ kHz, corresponding to the UHF FCC regulations ($\Delta f_{\max} = 26$ MHz). The sensor resolution using the FST method is

$$\Delta V_{\min} = \frac{\Delta V_{\max}}{52}. \tag{7}$$

In the case of the CST method, the range of usable capacitance values is bounded by the IC specifications, $\Delta\hat{C} = \hat{C}(V_{\max}) - \hat{C}(V_{\min})$, and it determines the sensor resolution of the CST method which can be expressed as

$$\Delta V_{\min} = \frac{\Delta V_{\max}}{N_c} \cdot \frac{C_{\max} - C_{\min}}{\hat{C}(V_{\max}) - \hat{C}(V_{\min})} = S_{\mathrm{CST}}^{-1} \cdot \Delta C_{\min} \tag{8}$$

where N_c is the number of discrete capacitance levels the self-tuning mechanism can select, $\Delta C_{\min} = ([\Delta C_{\max}]/N_c)$ is the resolution of the self-tuning mechanism, and $\Delta C_{\max} = C_{\max} - C_{\min}$ is the range of the self-tuning mechanism.

In terms of the sweat rate, the sensor range and resolution, for both FST and CST methods, can be computed as

$$q_{\max} = \frac{\Delta V_{\max}}{\Delta t} = \frac{V_{\mathrm{ch}}}{\Delta t} \tag{9}$$

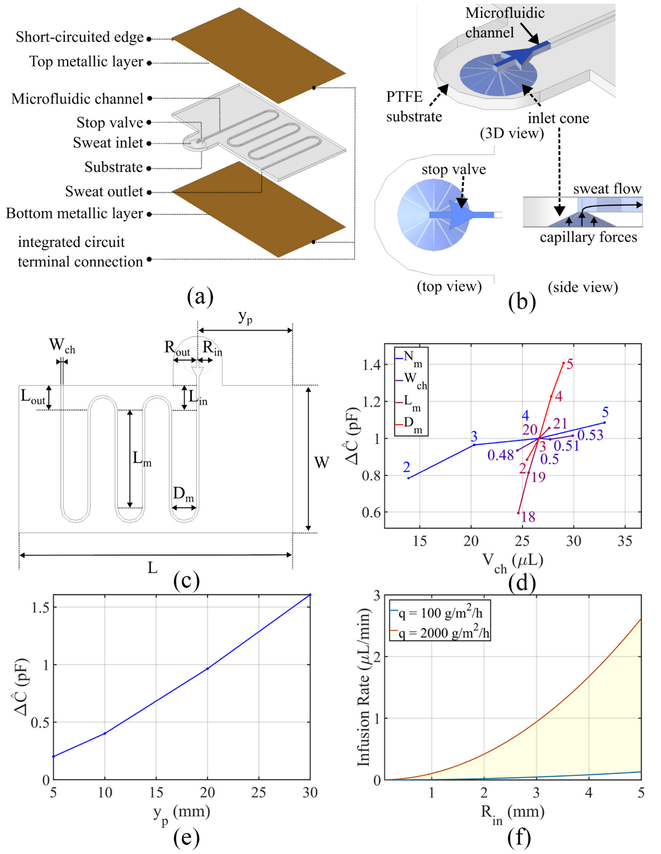

Fig. 1. ABS design. (a) Multilayered view of the proposed tag antenna. (b) Detail of the sweat inlet mechanized in the PTFE substrate. (c) Antenna geometrical parameters. (d) Sensor range for a variable V_{ch} depending on the channel geometrical parameters. (e) Sensor range for constant V_{ch}, depending on y_p. (f) Minimum and maximum infusion rates corresponding to the range of sweat rate of healthy individuals depending on the inlet radius R_{in}.

and

$$q_{\min} = \frac{\Delta V_{\min}}{\Delta t} = \frac{S^{-1}_{(\text{FST/CST})} \cdot \Delta\left(\hat{f}/\hat{C}\right)_{\min}}{\Delta t} \tag{10}$$

respectively.

III. ANTENNA DESIGN

The proposed antenna-based SLMD consists of a short-ended patch-like antenna with an embedded microfluidic channel that enables the interaction between the secreted sweat and the ABS [28]. This structure provides narrow band impedance matching, to achieve the required sensor resolution, and high selectivity, i.e., it is less affected by external phenomena than single layer antennas. Fig. 1(a) illustrates the sensor parts. A sweat inlet is built in a protruding part of the substrate. Sweat is excreted by the sweat glands under mild pressure. Then, it is passively drawn into the microfluidic channel through the sweat inlet by capillary action. Finally, it is evacuated through the sweat outlet. A detailed view of the sweat inlet is presented in Fig. 1(b).

The tag IC used in this work is the Axzon Magnus S3 [16] which can encode 485 capacitance levels effectively within a range of $\Delta C_{\max} = 2.9–1.9\,\text{pF} = 1\,\text{pF}$, corresponding to a resolution of $\Delta C_{\min} = (1\,\text{pF}/485) = 2.06\,\text{fF}$. The input impedance of the IC, $Z_{IC}(f, C)$, can be modeled as an RC parallel circuit, with a variable capacitance, C, [16].

The antenna design geometrical parameters are illustrated in Fig. 1(c). H is set to 1 mm to fit the application flexibility requirements. The channel is set to have a square cross section. Therefore, the channel thickness, H_{ch}, is equal to the channel width W_{ch}. L_m determines the length of the channel meanders, which, for a fixed L, also determines L_{in} and L_{out}. D_m controls the distribution of the N_m channel meanders along the length of the antenna, the separation between them and the distance between the sweat inlet and outlet. y_p controls the relative position of the channel with respect to the short-circuited edge. V_{ch} is the channel volume, which can be computed as

$$V_{\text{ch}} = \left(L_{\text{in}} + N_m \cdot L_m + (N_m - 1) \cdot \pi \cdot \frac{D_m + W_{\text{ch}}}{2} + L_{\text{out}}\right) \cdot H_{\text{ch}} \cdot W_{\text{ch}}. \tag{11}$$

The antenna design consists of an iterative process in which the designer has to 1) find the values of L and W that maximize τ in the upper margin of the capacitance range of the self-tuning mechanism ($\approx C_{\max} = 2.9$ pF) for the empty state (empty channel) and 2) modify the microfluidic channel geometrical parameters to produce the desired sensor range, i.e., achieving the best impedance matching in the lower margin of the capacitance range of the self-tuning mechanism ($\approx C_{\min} = 1.9$ pF) for the saturated state (channel full of sweat).

The effect of the microfluidic channel geometrical parameters is cumbersome and difficult to analyze with a naked eye. Consequently, a parametric analysis is presented next to provide the guidelines for designing the sensor microfluidic channel.

A. Parametric Analysis

The main goal of the microfluidic channel design process consists of tuning the channel geometrical parameters to adjust the sensor range to match the range of the self-tuning mechanism for maximizing the sensor resolution.

Simulations are conducted using pathwave EM design (EMPro) software. All simulations are performed starting from the geometrical parameters of the reference design: $L = 55.4$ mm, $W = 30$ mm, $H = 1$ mm, $R_{\text{in}} = 3$ mm, $R_{\text{out}} = 5$ mm, $L_{\text{in}} = L_{\text{out}} = 5$ mm, $N_m = 4$, $W_{\text{ch}} = 0.5$ mm, $H_{\text{ch}} = 0.5$ mm, $L_m = 20$ mm, $D_m = 3$ mm, and $y_p = 20$ mm. Only one geometrical parameter is changed at each simulation.

In the first part of the analysis, the variation of the sensor range with respect to V_{ch} is assessed for variations of the geometrical parameters. The results, in Fig. 1(d), show that all parameters produce an almost linear dependence of $\Delta\hat{C}$ with respect to V_{ch}. Parameters N_m and W_{ch} produce similar slopes corresponding to a small increase of the $\Delta\hat{C}$ with respect to V_{ch}. Instead, D_m and L_m have a stronger effect in the sensor range. In addition, D_m and L_m can be tuned to produce a large effect on $\Delta\hat{C}$ without breaking the antenna geometry.

Next, the reference design is simulated for different values of the channel position, y_p. The channel volume is fixed to

$V_{\mathrm{ch}} = 26.6\,\mu$L. Fig. 1(e) shows the almost linear dependence of $\Delta\hat{C}$ with y_p. Therefore, modifying y_p is a simple way to tune $\Delta\hat{C}$ without modifying V_{ch}.

Additional considerations include designing W_{ch} considering the integrity of the structure that must resist possible tensions and deformations. Moreover, the large variations produced by tuning y_p lead to an important conclusion: each of the meanders has a different impact in the sensor sensitivity depending on their position along the length of the antenna. In fact, the closer the meanders are to the feeding edge, the stronger the effects, caused by sweat reaching those parts, over the antenna input impedance. In conclusion, once the desired V_{ch} is chosen the geometrical parameters can be obtained to maximize the sensor range according to (11), Fig. 1(d) and (e).

The minimum and maximum infusion rates are defined so that the infusion rate divided by the inlet area matches the maximum and minimum sensible sweat rates of healthy individuals, $q_{\max} = 2000$ g/m^2/h and $q_{\min} = 100$ g/m^2/h, respectively, [7]. Fig. 1(f) shows the range of channel flow rates (yellow area) that can be used to track the human sweat rate, depending on R_{in}. For the proposed design $R_{\mathrm{in}} = 3$ mm, therefore, the infusion rates used in the following experiments will be limited between 0.2 and 1 μL/min.

B. Sensor Operation

The sensor operation, for the CST method, is validated through simulations considering different sweat volumes inside the microfluidic channel and the reference design. Fig. 2(a) illustrates the sequence of simulated cases for different sweat volumes, V, inside the microfluidic channel, from the empty state (0%) to the saturated state (100%) in steps of 25%.

In the empty state, the microfluidic channel has the dielectric properties of the air ($\varepsilon_r = 1.00058$, $\tan\delta \approx 0$) and, in the saturated state, it has the dielectric properties of sweat ($\varepsilon_r = 76$ and $\tan\delta = 0.3$ [29]). For intermediate states, the microfluidic channel is divided in two portions, the part connected to the sweat outlet which contains only air, and the part connected to the sweat inlet containing only sweat.

Fig. 2(b) and (c), respectively, show the IC input resistance ($R_{IC}(f, C)$) and reactance ($X_{IC}(f, C)$), reversed sign, for five equidistant capacitance values covering the range of operation ($\Delta C_{\max}$) of the self-tuning mechanism. Simulation results of the antenna resistance ($R_a(f, V)$) and the antenna reactance ($X_a(f, V)$) are also, respectively, plotted in Fig. 2(b) and (c). Results confirm that the variation of the sweat volume inside the microfluidic channel shifts the antenna input impedance, $Z_a(f, V)$, toward lower frequencies. Additionally, the high dielectric losses of sweat [30] increase the antenna loss resistance, which reduces the antenna gain and increases the input resistance.

Let us consider a sensor operating at $f_0 = 866.5$ MHz with a microfluidic channel containing a sweat volume V. The value of C selected by the IC self-tuning mechanism can be approximated as the value of C producing an IC reactance reversed sign, $-X_{IC}(f_0, C)$, intersecting the black vertical dashed line and the antenna reactance, $X_a(f_0, V)$ [c.f. Fig. 2(c)]. Fig. 2(d) shows the power transmission coefficient of the tag at f_0 as a function of the IC variable capacitance C. Each curve corresponds to a different sweat volume inside the microfluidic channel. The C values corresponding to the peaks of the curves are the ones being selected by the IC self-tuning mechanism. In this example, the empty state and the saturated state correspond to $C(0) = 2.87$ pF and $C(V_{\mathrm{ch}}) = 1.9$ pF, respectively.

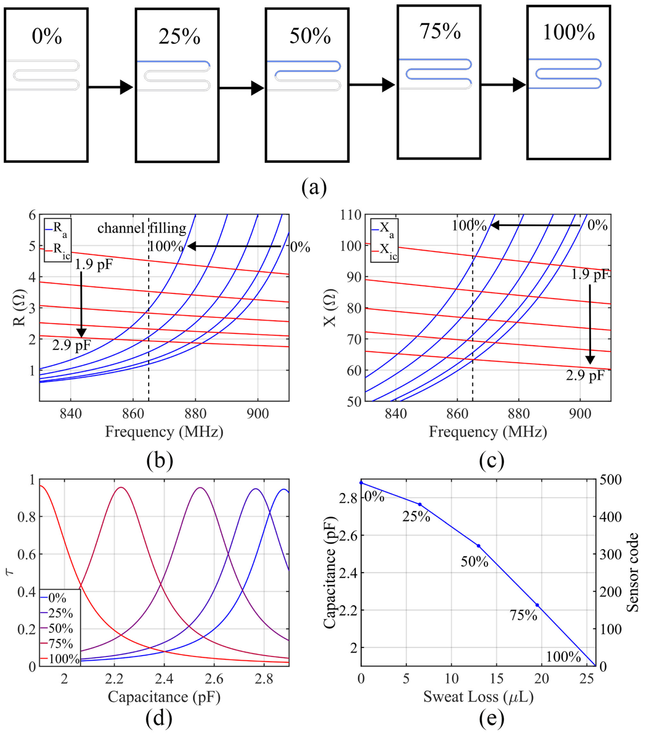

Fig. 2. Simulation results. (a) Sequence of increasing channel sweat volume levels corresponding to the five simulated cases. (b) Simulation results of the antenna input resistance (blue) for five sweat volumes and the IC input resistance (red) for five equidistant parallel capacitances. (c) Simulation results of the antenna input reactance (blue) for different sweat volumes and IC input reactance (red) for five equidistant parallel capacitances covering the range of the self-tuning mechanism (1.9–2.9 pF). (d) Power transmission coefficient obtained for the results of Fig. 2(b) and (c). (e) Capacitance and sensor-code extracted from the maximum values of the τ curves.

Next, the tag encodes the selected capacitance value as a sensor code and backscatters it for remote processing [12]. Fig. 2(e) shows the sensor codes obtained (right axis) for the simulated sweat volumes. The received sensor code can be mapped to the sweat loss per inlet area, using (5), and to the sweat rate (q), using (6).

IV. MEASUREMENTS

In this section, the sensor performance is evaluated through the measurement of the antenna S-parameters obtained using a FieldFox VNA from Keysight. The prototype dimensions have been adjusted to account for the difference observed between simulation and measurement results. The main source of mismatch is the low accuracy in obtaining the simulated channel height using a milling machine [Fig. 3(a)]. Variations of H_{ch} have a significant effect on V_{ch} (11). In consequence,

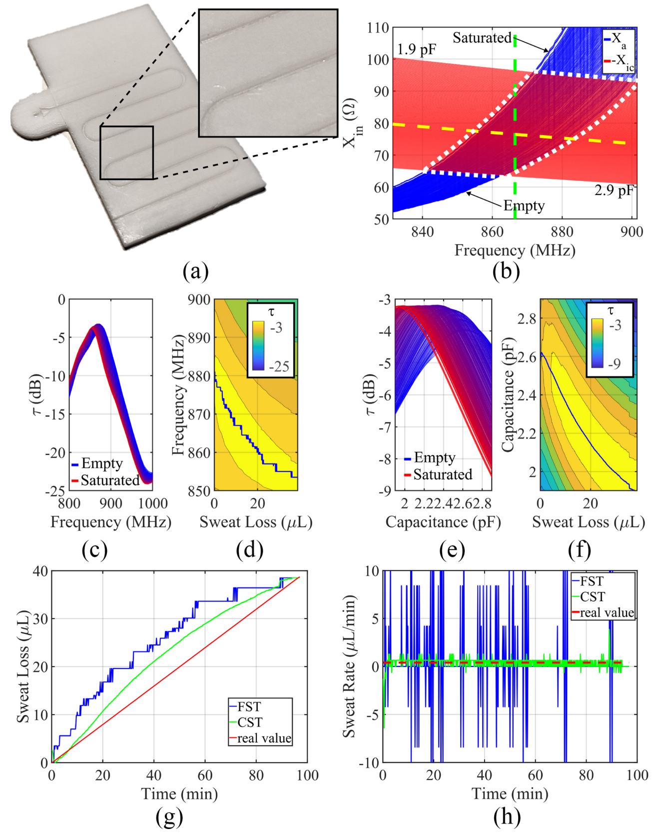

Fig. 3. Continuous VNA measurements during the channel sweat filling at a constant infusion rate of 0.4 μL/min. (a) Antenna input reactance for different V (blue) and IC input reactances reversed sign for the range of variable capacitances C. (b) Best matching frequency depending on C and V. (c) τ with respect to the frequency. (d) τ contour lines for a constant capacitance of 2.4 pF and $\tau_{\max}$ solid blue line. (e) τ with respect to the variable capacitance. (f) τ contour lines for a constant frequency of 865.5 MHz with respect to the capacitance and $\tau_{\max}$ solid blue line. (g) Comparison between the sweat loss values obtained through mapping the solid line of Fig. 3(d) using (3), mapping the solid line of Fig. 3(f) using (5), and the actual infusion rate. (h) Sweat rates of the FST and the CST computed using (2) and (6) respectively, and compared to the real value.

$\hat{f}$ and $\hat{C}$ can shift outside of the measurable ranges ($\Delta f_{\max}$ and $\Delta C_{\max}$). $\Delta\hat{f}$ and $\Delta\hat{C}$ can be also affected [Fig. 1(d)]. The antenna substrate, sweat inlet and microfluidic channel are mechanized in an 1 mm polytetrafluoroethylene (PTFE) slab using a milling machine. The metallic layers are built with adhesive copper tape. The final parameters are: $L = 55.3$ mm, $W = 30$ mm, $H = 1$ mm, $V_{\mathrm{ch}} = 38.39\,\mu$L, $N_m = 6$, $W_{\mathrm{ch}} = 0.5$ mm, $L_m = 20$ mm, $D_m = 3$ mm, and $y_p = 19$ mm. The S_{11} is continuously measured at intervals of 10 s ($\Delta t = 10$ s) while the Fusion 200-X syringe pump from Chemyx is used to inject artificial sweat into the microfluidic channel. The artificial sweat for the laboratory experiments is fabricated following the procedure detailed in [30].

A. Single-Flow Rate Measurements

The syringe pump is programmed for a constant infusion rate of 0.4 μL/min, which corresponds to 849 g/mm^2/h. The antenna input reactance is computed from S_{11} measurements and presented in Fig. 3(b). Blue curves represent the ABS measured input reactance $X_a(f, V)$ shifting from upper to lower frequencies in response to the increasing volume of artificial sweat inside the microfluidic channel. Red lines represent the IC input reactance reversed sign $-X_{IC}(f, C)$ for the different levels of the variable capacitance ($N_c = 485$ levels). The area surrounded by the white dotted line includes the points for which the IC self-tuning mechanism optimizes the complex conjugate impedance matching between the IC and the antenna input reactance, for all possible combinations of V and C.

The FST method is applied considering a bandwidth of 26 MHz and 52 channels. Fig. 3(c) shows the τ curves computed for the IC input impedance $Z_{IC}(f, C_0)$, corresponding to the yellow dashed line of Fig. 3(b) ($C_0 = 2.4$ pF), and the antenna input impedance $Z_a(f, V)$, for consecutive sweat volume increments [blue lines of Fig. 3(b)]. The same data is plotted in the planar contour graph of Fig. 3(d), where a τ curve is mapped to a vertical line, and the magnitude of the curve is represented using a color scale. This graph allows to draw the solid blue line tracking the frequencies corresponding to τ peaks (1) with respect to the elapsed infusion time. It's worth noticing that the proposed sensor design does not allow using the FST method in commercial readers due to the utilization of unregulated frequencies (854–880 MHz). However, the FST method can be applied in commercial readers in the FCC band by simply tuning the sensor impedance (decreasing the patch length L). A performance similar to the one measured in this study can be expected, given that the sensor operation has been already tested using the same bandwidth and number of channels.

The CST method is applied for $f_0 = 866.5$ MHz, which is marked with the vertical green dashed line in Fig. 3(a). The k_{th} τ curve is computed for the value of $Z_a(f = f_0, V = V_k)$, and all the values of $Z_{IC}(f = f_0, C)$, for $C_{\min} \leq C \leq C_{\max}$. Doing this for all V_k results in the τ curves plotted in Fig. 3(e). For each measurement (for each τ curve) the self-tuning mechanism will select the value of C that produces the maximum power transfer between the antenna and the IC, corresponding to the peak capacitance value (4) of the τ curve. The computed values of $\hat{C}$ are represented by a solid blue line in Fig. 3(f).

The values of $\hat{f}$ and $\hat{C}$ can be mapped to the measured sweat loss using (3) and (5) respectively. The results for both FST and CST methods are compared in Fig. 3(g), to the real sweat loss values. The comparison shows that the CST method achieves higher accuracy in tracking the sweat loss. Moreover, the higher resolution of the CST method has a dramatic effect on the estimation of the sweat rate, as shown in Fig. 3(h), with a resolution $q_{\min} = 0.47$ μL/min, compared to the 4.4 μL/min of the FST method, computed using (7)–(9). The sweat rates of the FST and the CST methods have been calculated using (2) and (6) respectively.

B. Multiflow Rate Measurements

Next, the sensor operation is assessed for a set of infusions rates covering the range of sweat rate of healthy individuals [see Fig. 1(f)] and the accuracy of the FST and the CST methods is compared.

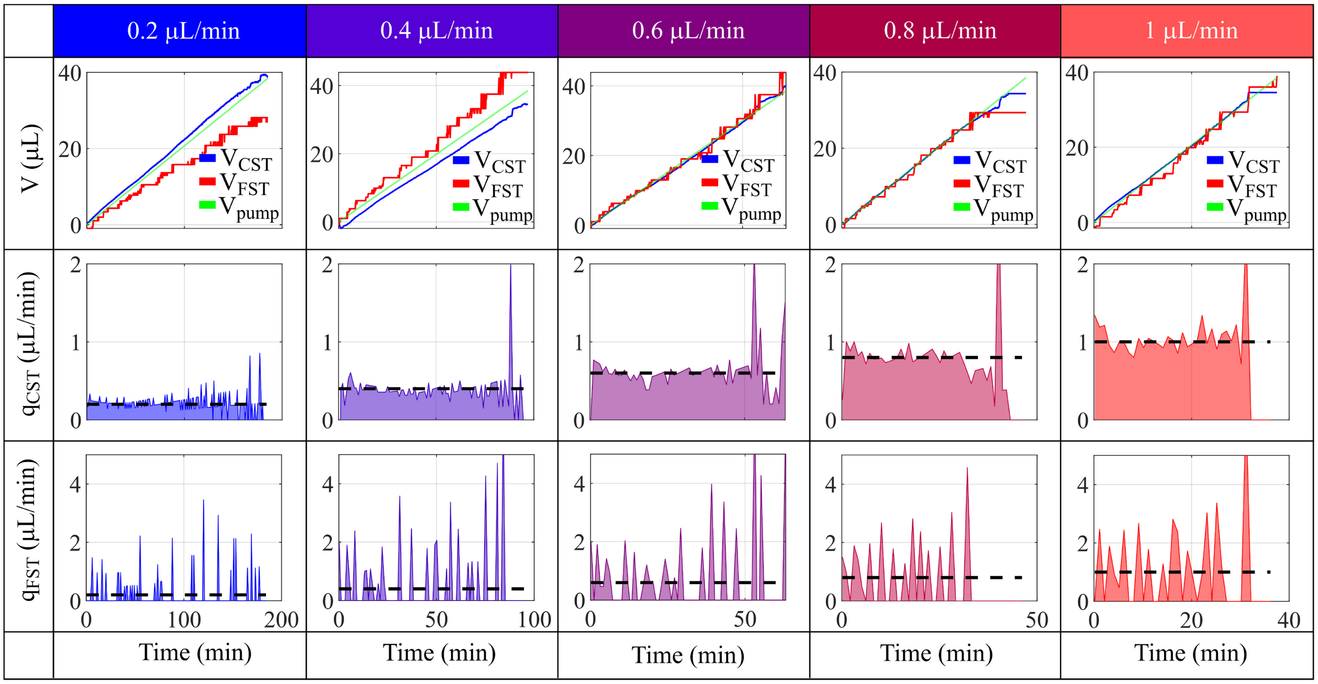

Fig. 4. Measurements at multiple infusion rates: sequence of graphs plotting the sweat loss and sweat rate measurements, where each column contains the graphs corresponding to a different infusion rate.

The measurements for all infusion rates are processed using both the CST and FST methods. Δt in (2) and (6) is set to 1 min to increase the resolution of the sweat rate estimation ($q_{\mathrm{CST}_{\min}} = 0.87\,\mu$L/min and $q_{\mathrm{CST}_{\min}} = 0.11\,\mu$L/min). The results, in Fig. 4, show that the sensor can track the infused sweat volume for all infusion rates using both methods. The CST method produces smoother curves, due to the higher resolution of the method, compared to the FST. The second and third rows of Fig. 4 consist of the sweat rate estimations (q_{CST}, q_{FST}) using both methods. While the FST method can not provide accurate results for the sweat rate estimation due to the low resolution of the method, the results show that the CST method can track the sweat rate reliably for all infusion rates. However, the presence of unexpected peaks near the end of the experiments suggests a low sensor accuracy in the lower end of sensor code range.

Fig. 5(a) and (b) shows the sweat loss errors for the first and third degree polynomial models, respectively. Results show that the third degree polynomial approximation reduces the error for both methods. The results show that the CST method with a third degree polynomial model [Fig. 5(b)] achieves an accuracy over 90% in the estimation of the sweat loss, for all the tested sweat rates. This represents a tremendous improvement, considering the low cost of the technology, the energy efficiency of the sensors, their simplicity and ease of integration.

Fig. 5(c) and (d) show that the FST (red) produces an error considerably higher than 100% for both the first and third degree polynomial models. The error of the sweat rate estimation using the CST method (blue) with a first degree polynomial model and the third degree polynomial model can be seen in Fig. 5(e) and (f), respectively. The figures show that the third degree polynomial achieves higher accuracy for most part of the experiments.

V. RFID EXPERIMENTS

This section presents the validation of the sensor through experiments using RFID readers in the laboratory environment and in a realistic scenario. For these experiments, the prototype is adjusted to maximize the sensor range and resolution. To that end the patch length has been decreased to $L = 52.5$ mm to shift the sensor response to higher frequencies and the separation between meanders has been increased ($D_m = 5$ mm) to increase the sensor range. Consequently, the microfluidic channel volume has increased to $V_{\mathrm{ch}} = 42.3\,\mu$L.

A. Laboratory Experiments

The prototype is tested using a commercial RFID reader module. The setup is illustrated in Fig. 6(a). The RFID reader consists of an m6e RFID reader module from JADAK connected to a Rapsberry pi 4 model B [31] operating in the ETSI band and continuously interrogating the tag at the frequency of 866.5 MHz. Like in the previous section, the sensor operation is tested for five different infusion rates using a syringe pump. The results corresponding to sweat loss measurements are displayed in Fig. 6(b). The green dashed lines correspond to the real infusion rates. The results show that the sensors can track the sweat loss with a small error. The sweat rate is also computed for the different infusion rates in Fig. 6(c). The estimation of the sweat rate average is determined for different time intervals and the results are plotted in Fig. 6(d). These results show that a low-cost commercial RFID system can be used to track the

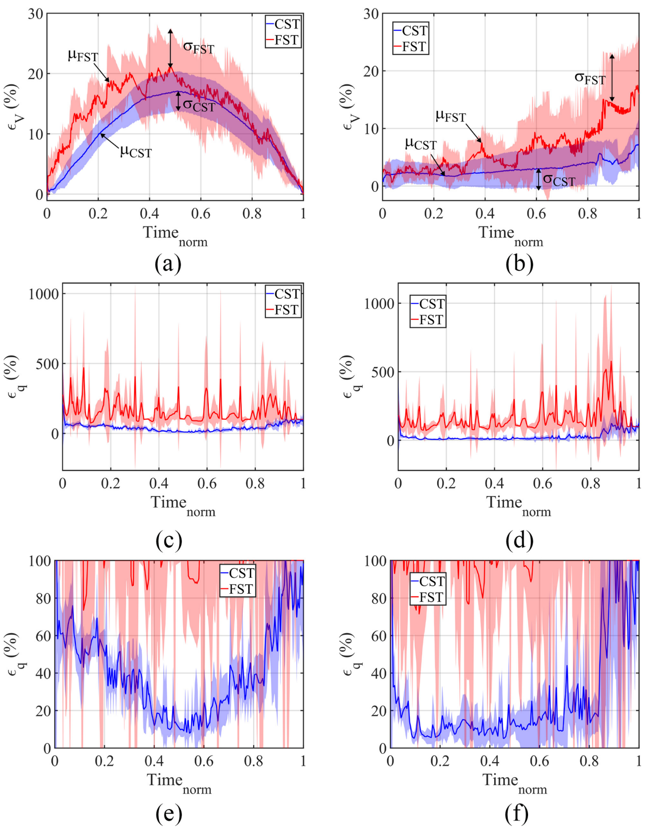

Fig. 5. Measurements at multiple infusion rates. (a) Mean and standard deviation of the sweat loss measurement error for the sensitivity using an, (a) first and (b) third degree polynomial model. Mean and standard deviation of the sweat rate measurement error for a (c) first and (d) third degree polynomial model. Zoom in of the *y*-axis of the sweat rate measurement error using an (e) first and (f) third degree polynomial model.

sweat loss and that the sweat rate average can be estimated with an accuracy over 95% by using time intervals longer than 5 s.

The sensor read range is measured using the Tagformance Pro. Measurements in free space (off-body) and on a human body (on-body) are conducted considering both the empty and saturated states of the microfluidic channel. The results are displayed in Fig. 6(e). Comparing the off-body (blue lines) and on-body (red lines) scenarios in the empty state, a frequency shift of 5 MHz to lower frequencies can be observed due to the higher relative permittivity of the human body. The read range increases from ≈2 m in the off-body scenario to ≈3 m in the on-body scenario due to the effect of the high electromagnetic losses of the human body in contact with the tag which modify the antenna input impedance and increase the power transmission coefficient τ.

Comparing the empty (thick lines) and saturated (thin lines) states, Fig. 6(e) shows that a small amount of sweat (42.3,μL) produces a large frequency shift of ≈ 50 MHz in both on-body and off-body scenarios, with a similar magnitude in both states. The combination of higher substrate losses due to the sweat with the IC self-tuning mechanism increase the tag power transmission coefficient (τ), compensating for the decrease in the antenna gain. Consequently, the read range of the proposed sensor in a realistic on-body scenario operating in the ETSI band is between 2 and 3 m.

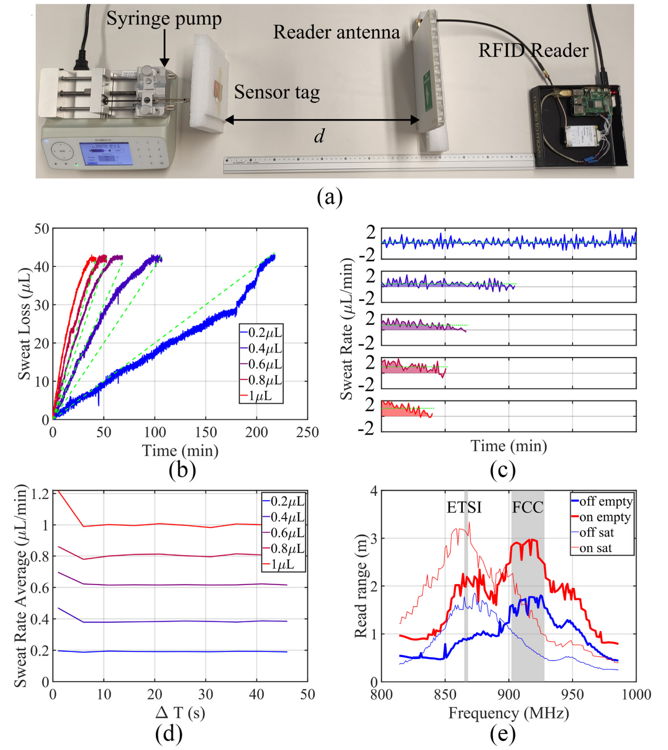

Fig. 6. Commercial RFID system measurements. (a) Measurement setup. (b) Sweat loss measurements for different infusion rates. (c) Sweat rate measurements for different infusion rates. (d) Average sweat rate values for different infusion rates and different time intervals for the sweat rate computation. (e) Read range measurements for on-body and off-body scenarios in the empty and saturated states.

B. Realistic Experiment

The sensor has been tested in a realistic environment through an experiment conducted on a stationary bicycle. The experiment setup is illustrated in Fig. 7(a). The sensor is placed on the chest of a human subject using a medical grade adhesive film (Tegaderm) [Fig. 7(b) and (c)]. The reader antenna is placed at a distance of 1.5 m from the subject. The adhesive film is carefully attached to avoid air bubbles at the edges of the sensor and ensure the sweat flows inside the sweat inlet [Fig. 7(c)]. The low-profile and flexibility of the sensor materials provide a comfortable adhesion to the body. The subject pedals at a continuous pace until the microfluidic channel is completely filled with sweat, corresponding to the lowest sensor code value.

The results of the sensor code returned by the tag are displayed in Fig. 7(d). The subject reported starting to sweat after 8 min. Accordingly, the sensor code remains stable during the first 8 min and it starts decreasing after that. A linear trend can be observed by visual inspection. However, the measurements are noisy due to changes in the distance and orientation of the tag with respect to the reader antenna. The sweat volume has been computed from the sensor code using (5). The results in Fig. 7(e), show that the same linear trend, corresponding to an almost constant sweat rate, can be

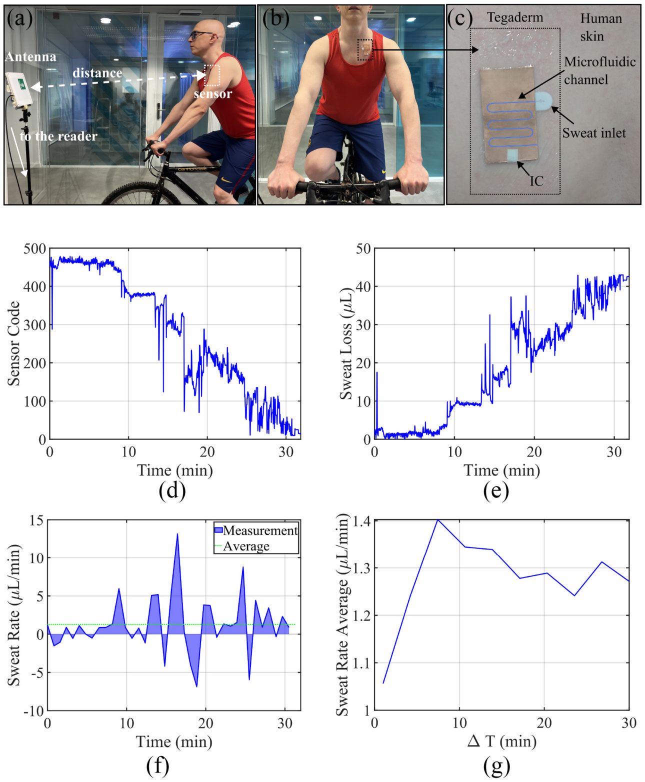

Fig. 7. Realistic experiments. (a) Experiment setup. (b) Sensor prototype attached to a human torso (on-body) during the experiment. (c) Sensor prototype attached to the human skin. (d) Sensor code returned by the tag. (e) Sweat loss measurements for different infusion rates. (f) Sweat rate measurements for different infusion rates. (g) Average sweat rate values for different infusion rates and different time intervals for the sweat rate computation.

observed through visual inspection. The error in the sweat loss measurement has a stronger effect in the sweat rate estimation [Fig. 7(f)] which results in a large error similar to the results obtained with the FST method. However, Fig. 7(g) shows that the sensor is still able to capture the sweat rate average in a realistic scenario.

VI. CONCLUSION

This contribution presents a cost-efficient sweat rate sensor that does not require batteries. The sensor consists of a low-cost passive UHF RFID tag comprising a standard self-tuning IC and a customized patch-like antenna where a microfluidic channel has been mechanized. The development of the equations that allow estimating the sweat loss and sweat range using an UHF RFID tag is carried out for the first time. This work also includes a parametric analysis providing the guidelines for optimizing the sensor range, resolution, and accuracy.

Two methods for the estimation of the sweat loss have been tested and compared: 1) the FST method consisting of tracking the frequency shift of the tag response and 2) the CST method consisting of tracking the sensor code, corresponding to the value of the variable capacitance selected by the IC self-tuning mechanism, backscattered by the tag. The CST method has demonstrated to achieve higher accuracy in both sweat loss and sweat rate measurements.

While low-cost technologies usually come with the counterpart of low accuracy, the proposed sensor achieves an accuracy over 90% in the estimation of the sweat loss using a third-degree polynomial model of the sensor response and the CST method. The results also prove that the average sweat rate can be estimated using a commercial UHF RFID system with an accuracy over 95% in the range of sweat rate values typical of healthy individuals.

This contribution demonstrates that sweat loss measurement devices can be implemented using cost-efficient, standard technologies, such as passive UHF RFID. This makes the proposed device a promising solution for enhancing and democratizing eHealth services for the general population.

REFERENCES

[1] Z. Jiang et al., “Fall detection systems for Internet of Medical Things based on wearable sensors: A review,” *IEEE Internet Things J.*, vol. 11, no. 21, pp. 34797–34810, Nov. 2024.

[2] A. Kos and A. Umek, “Wearable sensor devices for prevention and rehabilitation in healthcare: Swimming exercise with real-time therapist feedback,” *IEEE Internet Things J.*, vol. 6, no. 2, pp. 1331–1341, Apr. 2019.

[3] J. Rumbut, H. Fang, S. Carreiro, D. Smelson, and E. Boyer, “An overview of wearable biosensor systems for real-time substance use detection,” *IEEE Internet Things J.*, vol. 9, no. 23, pp. 23405–23415, Dec. 2022.

[4] N. Rashid, T. Mortlock, and M. A. A. Faruque, “Stress detection using context-aware sensor fusion from wearable devices,” *IEEE Internet Things J.*, vol. 10, no. 16, pp. 14114–14127, Aug. 2023.

[5] W. Xu, L. Hong, J. Zheng, M. Li, Y. Hua, and X. Zhao, “Wearable smart sensor system for monitoring and intelligent prediction of sodium ions in human perspiration,” *IEEE Internet Things J.*, vol. 11, no. 5, pp. 8146–8155, Mar. 2024.

[6] K. Kwon et al., “An on-skin platform for wireless monitoring of flow rate, cumulative loss and temperature of sweat in real time,” *Nat. Electron.*, vol. 4, no. 4, pp. 302–312, Mar. 2021.

[7] B. Zhong, K. Jiang, L. Wang, and G. Shen, “Wearable sweat loss measuring devices: From the role of sweat loss to advanced mechanisms and designs,” *Adv. Sci.*, vol. 9, pp. 1–27, Jan. 2022.

[8] A. Aggarwal, M. Dautta, L. F. Ayala-Cardona, A. Wudaru, and A. Javey, “Wearable humidity sensor for continuous sweat rate monitoring,” *Adv. Mater. Technol.*, vol. 8, no. 17, 2023, Art. no. 2300385.

[9] M. Liu et al., “Adaptively resettable microfluidic patch for sweat rate and electrolytes detection,” *Biosens. Bioelectron.*, vol. 257, Aug. 2024, Art. no. 116299.

[10] M. M. Butt et al., “Ambient IoT: A missing link in 3GPP IoT devices landscape,” *IEEE Internet Things Mag.*, vol. 7, no. 2, pp. 85–92, Mar. 2024.

[11] C. Occhiuzzi, S. Caizzone, and G. Marrocco, “Passive UHF RFID antennas for sensing applications: Principles, methods, and classifcations,” *IEEE Antennas Propag. Mag.*, vol. 55, no. 6, pp. 14–34, Dec. 2013.

[12] M. C. Caccami and G. Marrocco, “Electromagnetic modeling of self-tuning RFID sensor antennas in linear and nonlinear regimes,” *IEEE Trans. Antennas Propag.*, vol. 66, no. 6, pp. 2779–2787, Jun. 2018.

[13] F. Nanni and G. Marrocco, “Constrained design of potentiometric RFID sensors based on auto-tuning ICs,” *IEEE Sensors J.*, vol. 23, no. 3, pp. 3050–3058, Feb. 2023.

[14] F. Naccarata, M. Di Cristofano, and G. Marrocco, “Continuous detection of fluid leaks into the body by means of partially dissolvable antennas,” *IEEE J. Electromagn., RF Microw. Med. Biol.*, vol. 8, no. 1, pp. 15–25, Mar. 2024.

[15] A. Mostaccio, F. Naccarata, F. M. C. Nanni, J. Filippi, E. Martinelli, and G. Marrocco, “Soft and flexible wireless epidermal plaster made by laser-induced graphene,” *IEEE Sensors Lett.*, vol. 8, no. 7, pp. 1–4, Jul. 2024.

[16] "Magnus-S3 M3D passive sensor IC." Accessed: Oct. 5, 2024. [Online]. Available: https://axzon-docs-public.s3.us-east-2.amazonaws.com/docs/DS003F12+Axzon+Magnus+S3+M3D+datasheet.pdf

[17] T. Saha, S. Mukherjee, M. D. Dickey, and O. D. Velev, "Harvesting and manipulating sweat and interstitial fluid in microfluidic devices," *Lab Chip*, vol. 24, pp. 1244–1265, Jan. 2024.

[18] J. Song and J. Huang, "A microfluidic antenna-sensor for contactless characterization of complex permittivity of liquids," *IEEE Sensors J.*, vol. 23, no. 2, pp. 27251–27261, Nov. 2023.

[19] M. H. Zarifi, H. Sadabadi, S. H. Hejazi, M. Daneshmand, and A. Sanati-Nezhad, "Noncontact and nonintrusive microwave-microfluidic flow sensor for energy and biomedical engineering," *Sci. Rep.*, vol. 8, no. 1, p. 139, Jan. 2018.

[20] B. S. Cook, J. R. Cooper, and M. M. Tentzeris, "An inkjet-printed microfluidic RFID-enabled platform for wireless lab-on-chip applications," *IEEE Trans. Microw. Theory Techn.*, vol. 61, no. 12, pp. 4714–4723, Dec. 2013.

[21] L. Zhu, W. Li, X. Han, and Y. Peng, "Microfluidic flexible substrate integrated microstrip antenna sensor for sensing of moisture content in lubricating oil," *Int. J. Antennas Propagat.*, vol. 2020, no. 1, 2020, Art. no. 9675847.

[22] G. M. Bianco and G. Marrocco, "Joint design of self-tuning UHF RFID antenna and microfluidic channel for liquid sensing," *IEEE J. Radio Freq. Identif.*, vol. 8, pp. 58–67, 2024.

[23] "Tagformance pro—Leading RFiD test and measurement system." Voyantic.com. Accessed: Oct. 2, 2024. [Online]. Available: https://voyantic.com/lab/tagformance-pro/

[24] G. Marrocco, "The art of UHF RFID antenna design: Impedance-matching and size-reduction techniques," *IEEE Antennas Propag. Mag.*, vol. 50, no. 1, pp. 66–79, Feb. 2008.

[25] S. Lopez-Soriano and J. Parrón, "Performance assessment of a novel miniaturized RFID tag for inventorying and tracking metallic tools," *IEEE J. Radio Freq. Identif.*, vol. 2, no. 3, pp. 127–133, Sep. 2018.

[26] S. Lopez-Soriano, I. Spassovsky, J. Parrón, and G. Marrocco, "A passive wireless sensor network for temperature mapping inside a shielded coaxial enclosure," *IEEE J. Radio Freq. Identif.*, vol. 2, no. 3, pp. 144–151, Sep. 2018.

[27] P. J. Pritchard and J. W. Mitchell, *Fox and McDonald's Introduction to Fluid Mechanics*, 9th ed. Nashville, TN, USA: Wiley, Mar. 2015.

[28] S. López-Soriano, X. Vilajosana, and J. Melià-Seguí, "A battery-less and low-cost RFID sensor for unassisted multilevel detection of sweat loss," *IEEE Sensors J.*, vol. 24, no. 24, pp. 42028–42037, Dec. 2024.

[29] A. R. Eldamak, S. Thorson, and E. C. Fear, "Study of the dielectric properties of artificial sweat mixtures at microwave frequencies," *Biosensors*, vol. 10, no. 6, p. 62, Jun. 2020.

[30] J. Melià-Seguí, R. B. S. López-Soriano, X. Vilajosana, and S. Sarma, "Low-cost RFID-based sensor integrated in textile for noninvasive pervasive hydration monitoring," *IEEE Sensors J.*, early access, Dec. 8, 2023.

[31] S. López-Soriano, J. Melià-Seguí, and J. Parrón, "A durable and flexible, low-cost tag antenna design for UHF RFID wearable applications," in *Proc. IEEE 13th Int. Conf. RFID Technol. Appl. (RFID-TA)*, 2023, pp. 9–12.

Sergio López-Soriano (Member, IEEE) received the M.Sc. degree in micro and nanoelectronics engineering and the Ph.D. degree in electronics and telecommunication engineering from the Universitat Autónoma de Barcelona, Bellaterra, Spain, in 2013 and 2018, respectively.

He was enrolled with the Scatterer ID Project, LCIS Laboratoire, Valence, France, from 2018 to 2019. He was with the Ubiquitous Computing Lab, Universitat Pompeu Fabra, Barcelona, Spain, from 2019 to 2022, as a Postdoctoral Researcher of Robotics. He is currently with the Wireless Network Group, Universitat Oberta de Catalunya, Barcelona. He has been an Assistant Lecturer with the Universitat Autónoma de Barcelona since 2019. His current research interests include RFID sensors, antenna design, and ambient Internet of Things.

Josep Parrón Granados was born in Sabadell, Spain, in 1970. He received the M.S. degree in telecommunication engineering and the Ph.D. degree from the Universitat Politécnica de Catalunya, Barcelona, Spain, in 1994 and 2001, respectively.

From 2000 to 2002, he belonged to the Electromagnetic and Photonic Engineering Group, Signal Theory and Communication Department, UPC, as an Assistant Professor. Since 2002, he has been a Lecturer with the Telecommunication and Systems Engineering Department, Universitat Autónoma de Barcelona, Bellaterra, Spain. He has co-authored 34 technical peer-reviewed journal papers and over 90 conference contributions. His current research interests include numerical methods for electromagnetism, antenna analysis and design, phased arrays, and reflective intelligent surfaces.

Joan Meliá-Seguí (Senior Member, IEEE) received the B.Sc. and M.Sc. degrees in telecommunications engineering from the Universitat Politécnica de Catalunya, Barcelona, Spain, in 2003 and 2005, respectively, and the Ph.D. degree from the Universitat Oberta de Catalunya, Barcelona, (UOC), in 2011.

He has been a Researcher with Universitat Pompeu Fabra, Barcelona; a Visiting Researcher with Palo Alto Research Centre (Xerox PARC), Palo Alto, CA, USA; and a Fulbright Visiting Scholar with Massachusetts Institute of Technology, Cambridge, MA, USA. He is currently an Associate Professor with the Faculty of Computer Science, Multimedia and Telecommunication Engineering, UOC. He has authored over 40 technical peer-reviewed publications. His research interests include low-cost RFID sensors and antenna-based sensing.